Two-dimensional metal-chalcogenide films in tunable optical microcavities: Supporting Information

S.Schwarz,[*,†] S. Dufferwiel,[†] P. M. Walker,[*,†] F. Withers,[‡] A. A. P. Trichet,[¶] M. Sich,[†] F. Li,[†] E. A. Chekhovich,[†] D. N. Borisenko,[§] N. N. Kolesnikov,[§] K. S. Novoselov,[‡] M. S. Skolnick,[†] J. M. Smith,[¶] D. N. Krizhanovskii,[†] and A. I. Tartakovskii[*,†]

Department of Physics and Astronomy, University of Sheffield, Sheffield S3 7RH, UK, School of Physics and Astronomy, University of Manchester, Manchester M13 9PL, UK, Department of Materials, University of Oxford, Parks Road, Oxford OX1 3PH, UK, and Institute of Solid State Physics, Russian Academy of Sciences, Chernogolovka 142432, Russia

E-mail: s.schwarz@sheffield.ac.uk; p.m.walker@sheffield.ac.uk; a.tartakovskii@sheffield.ac.uk

Abstract

In this Supplementary Information we present additional details for the sample and device design and fabrication, further characterization data for the microcavities used in the experiments, and, finally, detailed account of the results of FDTD calculations of the optical modes in the external cavity devices used in our work.

[*]To whom correspondence should be addressed
[†]University of Sheffield
[‡]University of Manchester
[¶]University of Oxford
[§]Institute of Solid State Physics

Microcavity fabrication and optical properties

Thin film fabrication

Monolayer MoS_2 and thin sheets of GaSe have been obtained by mechanical cleavage of bulk crystals. GaSe films were deposited straight from the wafer dicing tape on the flat DBR substrate, whereas the MoS_2 films were first deposited on a polymer layer and then transferred onto the flat DBR using standard transfer techniques.[1] Fig.1(a) shows a microscope image of a thin film of MoS_2. Areas with a single- and multiple-monolayer thicknesses can be distinguished on the graph from different shades of green color. The thickness of the films was further verified using atomic force microscopy. As seen on the graph the lateral dimensions of the single-monolayer part of the film exceed 50 μm by 50 μm. For GaSe films, flakes with sizes varying from 10 μm to 50 μm could be achieved. Our study is focused on relatively thick GaSe films with thicknesses ranging from 30 nm to 100 nm. We find that the PL intensity in GaSe films increases dramatically with the increase of the film thickness.

Mirror design and fabrication

The open-access microcavity fabrication consists of a two-step process[2,3]. First, the templates of concave mirrors are fabricated using a focused ion beam (FIB) machine (FIB200 from FEI). In this process, gallium ions are fired onto a precisely selected position of a silica substrate for a certain period of time referred to as the 'dwell time'. By adapting the dwell time as a function of the position of the ion beam, we create concave templates with various radii of curvature ranging from 1.7 μm to 25 μm onto a single chip. The template dimensions are measured by AFM. The smallest optically active cavities obtained so far had a radius of curvature of 5.6 μm. The efficiency of the FIB approach relies on the smallest achievable ion beam diameter, which in our case was down to 5 nm. The rms roughness of the template surface was found to be below 1 nm. During the second step, both the substrate with the concave mirrors and another flat silica substrate are coated with dielectric distributed Bragg

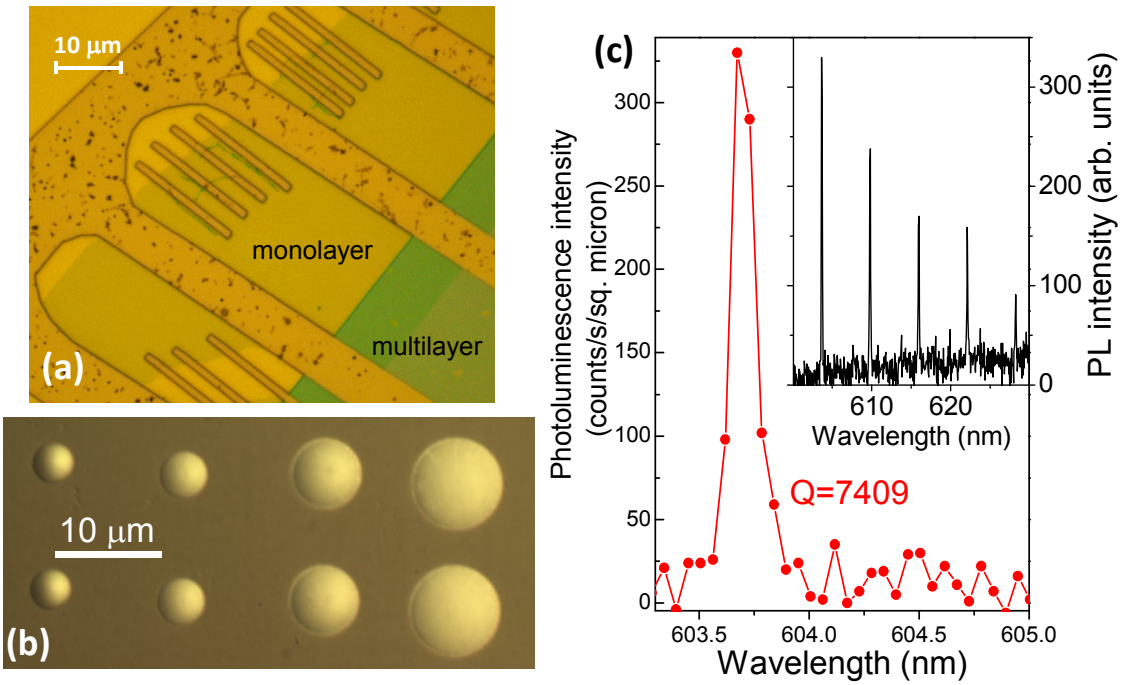

Figure 1: (a) Microscope image of a MoS_2 thin film deposited on a flat DBR. The monolayer and multilayer parts of the flake are marked. The film is held in position by several gold bars a few tens of nm thick (seen in yellow on the image). (b) Microscope image of a glass plinth with concave mirrors. Concave features with different radii of curvature are milled into a quartz substrate using focused ion beam, and are then covered with ten SiO_2/TiO_2 quarter-wavelength layer pairs, forming a distributed Bragg reflector. (c) PL spectrum measured in a microcavity containing a thin GaSe film (43 nm). A high Q-factor of around 7400 is observed for a longitudinal mode. The inset shows the same PL spectrum in a wide range of wavelength, where other modes with non-zero transverse mode numbers ($m, n \neq 0$) are observed.

reflectors (DBRs) comprising ten layers of SiO_2/TiO_2 (with refractive indexes 1.4 and 2.1, respectively) with layer thicknesses tuned to achieve maximum reflectivity at 650 nm. A microscope image of a typical substrate with concave mirrors is shown in Fig.1(b).

Measurement of high Q-factor modes in PL

Fig.1(c) shows photoluminescence (PL) spectra for a cavity comprising a thin GaSe film (43 nm) and having the highest Q-factor that we have measured in our devices. As shown in the main panel of the figure, here a longitudinal mode of the cavity has a Q-factor of ≈7400. This mode has a wavelength $\lambda_{q,m,n} = 603.7$nm. Here q=15 and m, n=0 (see Eq.1 in the main

text for the dependence of the resonant wavelength on q, m and n). The inset also shows the modes with q=14 and $m, n \neq 0$ observed in a broader spectral range. The measurements are carried out at a temperature of 4.2K using laser excitation at 532 nm in a cavity with L_{cav} =3.25μm and the radius of curvature of the top mirror R_c =25μm.

FDTD calculations of the cavity modes

Collection optics considerations

The ratio of observed intensities for the structure with and without the top mirror depends to some extent on the collection optics since the angular distribution of emission for a given wavelength of light is different for the two cases. The objective lens which collects the light is 7.5mm above the sample. This is sufficiently far from the sample compared to the wavelength of light and to the experimentally measured spot sizes that it can be considered to be in the far field. The collection efficiency is then entirely determined by the lens numerical aperture. The clear aperture of the objective is 4.5mm so only light emitted within $\pm$ 16.7 degrees is collected. To calculate the fraction of light collected it is necessary to know the power radiated per unit solid angle as a function of observation angle in the far field, the so-called radiation patterns.[4] Then the power emitted within the collection range of the lens may be compared with the total emitted power. Finally, comparison of the fraction of collected power may be made between the cases with and without top mirror to obtain the collection enhancement due to directionality of the cavity modes.

Radiation pattern for electric dipoles on a flat DBR

We consider first the radiation pattern without the top mirror. The bottom DBR mirror is modelled as a lossless dielectric multilayer consisting of 10 repeats of materials with refractive indexes 1.4 and 2.05 and thicknesses 116.07nm and 79.27nm respectively. The low index material faces the collection lens with the emitters positioned at zero separation from it.

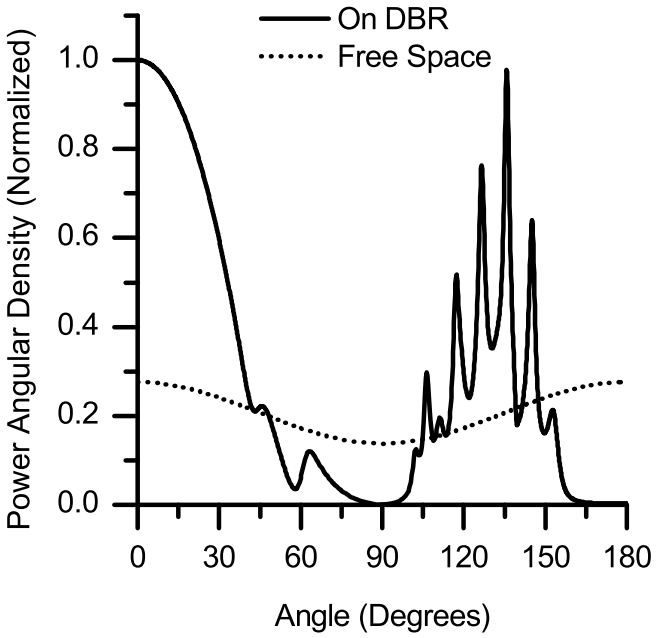

Figure 2: Dependence of emitted power per unit solid angle on observation angle in air for randomly oriented dipoles in the x-y plane on the DBR and in free space. Both curves have been normalised to the peak value for dipoles on the DBR.

The bottom of the DBR rests on a semi-infinite glass substrate with refractive index 1.54. The coordinate axes are chosen so that the layer planes are perpendicular to the z-axis. The emission from the sample may be modelled by an incoherent ensemble of classical electric point dipole current sources. Since in this work the excitons are two-dimensional it is assumed that the emitters are oriented randomly in the plane of the monolayer material. To model the random distribution of in-plane polarisations one may take the incoherent sum of the radiation patterns due to any two orthogonally polarised in-plane dipoles. The resulting total radiation pattern must then have circular symmetry about the z axis since there is no preferred azimuthal direction. As the spot size is small it is sufficient to treat only dipoles positioned at the origin $r = 0$ as the radial position will have little effect on the angular spread of the emission. Calculations are performed for dipoles radiating at a frequency corresponding to a wavelength of 680 nm in free space, as in the experiment. We follow the method presented in references.[4,5] The electric field due to a point electric dipole current

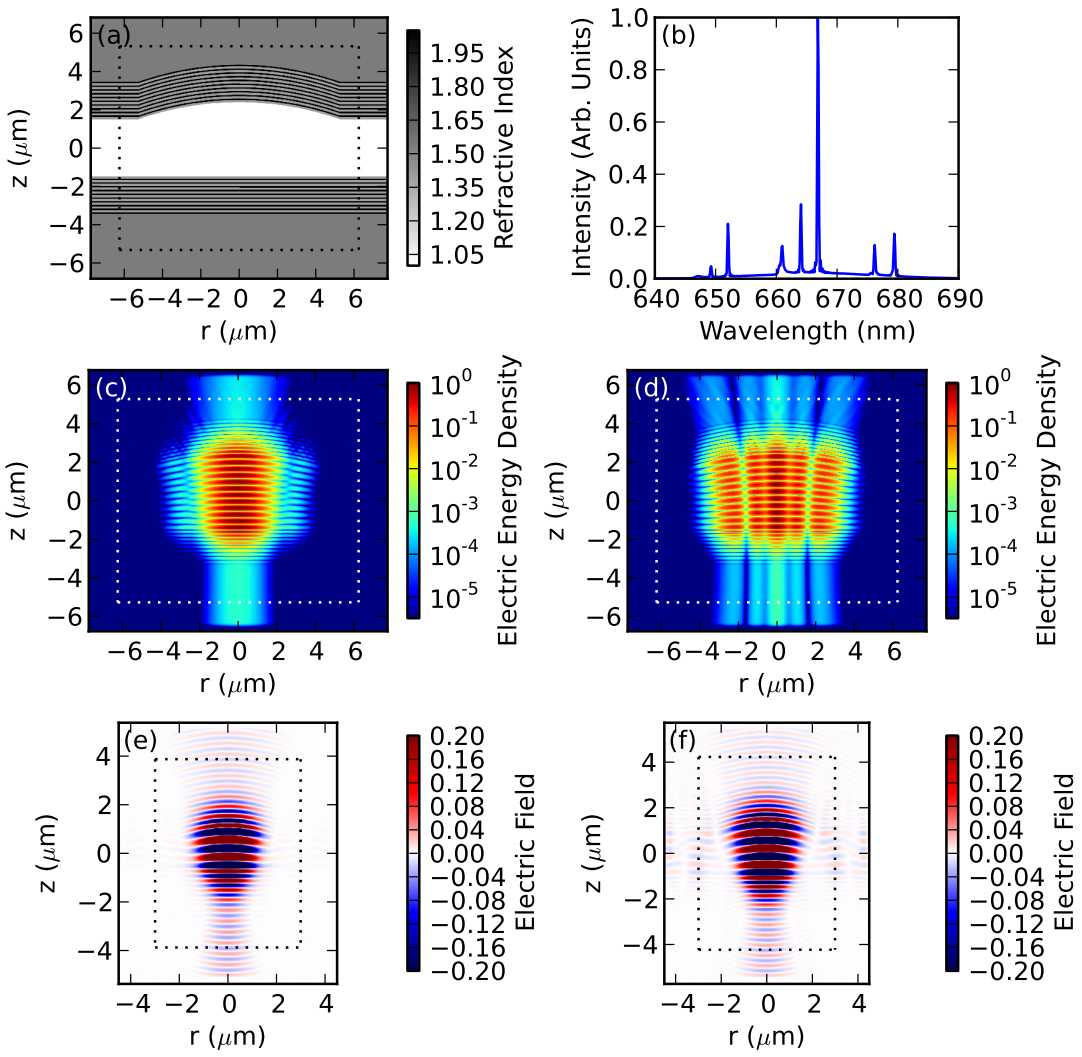

Figure 3: (a) Dielectric profile of cavity with 16μm radius of curvature mirror used in FDTD simulation. The dotted lines show the position of flux planes used to monitor the energy flux out of the structure. (b) Emission spectrum from the structure in (a) after excitation with a broadband source. (c,d) Electric density $E \cdot E^*$ for two modes in (b) on a logarithmic colour scale. (e,f) Radial electric field component on an exaggerated colour scale for 5.6μm radius of curvature cavities with mirror separations 1.12 and 1.82 respectively.

radiating in free space may be expanded in a basis of plane-waves. In the presence of the mirror the total upwards-radiating field (towards the collection lens) is the coherent sum of the radiation field emitted upwards by the dipole and the reflection from the mirror of the

field emitted downwards by the dipole. The free-space fields are separated into components with TE and TM polarisation with respect to the planar multilayer and the amplitude reflection coefficients are calculated using a transfer matrix technique.

Figure 2 shows the sum of radiation patterns due to x and y polarised dipoles for the case of dipoles in free space and directly on top of the DBR. For zero angle the DBR reflective phase is close to zero so the reflection reinforces the upward propagating wave and the upwards emission is enhanced with respect to free space. At larger angles the reflective phase increases so that the reflection begins to interfere destructively with the directly radiated field. For angles greater than 90 degrees the radiation is into the substrate. Very little power is radiated into modes close to 180 degrees because the DBR reflects them. For angles greater than 20 degrees from the negative z-axis, however, the DBR becomes ineffective and light is lost into the substrate. To obtain total power radiated in the range of polar angles $0 \leq \theta \leq \theta_{max}$ the radiation patterns must be integrated with azimuthal and polar collection angles according to $P(\theta_{max}) = \int_0^{2\pi} \int_0^{\theta_{max}} p(\theta, \phi) sin(\theta) d\theta d\phi$ where $sin(\theta) d\theta d\phi$ is the differential element of solid angle. Overall, 49% of the total radiation is emitted in the upwards direction and 9% is emitted within $\pm$16.7 degrees. This compares to only 3% emitted within $\pm$16.7 degrees for dipoles in free space.

Modes in a cavity with a concave DBR

When the top mirror is present a cavity is formed which confines electromagnetic modes at certain frequencies in all three dimensions. At these resonant frequencies the fields and hence the angular spread of the emission are determined by the cavity geometry. Simulations of the electromagnetic fields associated with the resonant cavity modes were performed with the finite-difference time-domain (FDTD) method, using a freely available software package.[6] The fields were first determined in the near-field zone close to the cavity. Simulations were performed in a cylindrical geometry on a two-dimensional grid of radial r and axial position z. This allowed much faster simulation times than a full three-dimensional calculation, which

was necessary due to the rather small 10 nm grid resolution used to accurately represent the cavity layers and top mirror curvature.

Figure 3(a) shows a schematic of the dielectric profile used for the simulations. The lower DBR is the same as in the planar case discussed earlier. The upper DBR is of the same structure as the lower DBR with low index material adjacent to the cavity. In the radial range $0 \leq r \leq r_m$, where r_m is the mirror radius, the DBR structure was offset in the positive z-direction according to $z = z_0 + \sqrt{R_c^2 - r^2} - \sqrt{R_c^2 - r_m^2}$ where R_c is the radius of curvature.

The separation between the upper and lower mirrors was first set to the experimentally estimated value and then refined in the following way. At the start of the simulation a broad frequency spectrum of electromagnetic radiation was excited by an electric dipole current source with short Gaussian temporal profile positioned on top of the lower DBR at $r = 400$nm. The electromagnetic energy flux passing through a box surrounding the structure (denoted by dotted lines in Fig. 3(a)) was collected for a sufficiently long time to allow all the energy to leave the simulation region. The flux was Fourier transformed to obtain a spectrum of the radiation emitted by the structure. Such a spectrum is shown in Figure 3(b). The sharp peaks identify resonant cavity modes and correspond to modes with a range of longitudinal (z-direction) and transverse (radial) quantization numbers.

Table 1: Simulation Parameters and Results

Cavity	Radius of curvature (μm)	Mirror Separation (μm)	Mode Wavelength (nm)	Quality Factor	Power Collected (%)
C1	16	2.98	679.8	11000	47
C2	10	2.05	681.1	7700	44
C3	5.6	1.82	678.9	4700	20
C4	5.6	1.12	678.1	5500	31
C5	5.6	2.52	679.9	1900	6

To find the fundamental (zero transverse quantization number) mode the simulation was repeated a number of times using a narrow-band excitation centered on each cavity mode in the spectrum. The cavity modes have a high quality factor Q and so decay much more

slowly than other transient fields caused by the excitation. After several decay-times of the chosen cavity mode the remaining electric and magnetic fields may be considered to have an approximately single-frequency harmonic time dependence and to represent the spatial dependence of the chosen cavity mode. Simulations were run for between one and three decay times $\tau = Q/\omega$ in order to reach this condition. After this the electric and magnetic fields at all points in the simulation volume were output. Figures 3(c-d) show the spatial profiles of the time-averaged electric intensity $E \cdot E^*$ for two of the modes in the spectrum corresponding to the longitudinal mode (c) and a mode with non-zero radial quantization number (d). The mirror separation was then adjusted slightly to bring the fundamental mode close to the experimental wavelength before the fundamental mode field profile was recalculated.

Figures 3(e-f) show the radial component of electric field as a function of position for two different mirror separations and 5.6μm radii of curvature. As can be seen from Fig. 3(c,e) the upwards radiation forms a beam centered about $r = 0$ which falls off to negligible intensity by the edge of the top flux plane. Comparing the fields above and below the structure we see that the curvature of the top mirror has a lensing effect which makes the beam propagating from the top of the sample spread more compared to that from the bottom. To obtain the relevant portion of the radiation pattern the total energy flux through the four flux planes was first examined and the fraction passing through the top compared to the total obtained. The field above the structure was then Fourier transformed to determine the spread of upwards power among waves propagating with different in-plane wavevectors and hence at different angles. Finally, these were integrated in the same manner discussed above for the case without top mirror. The input parameters and simulation results are summarised in Table 1.

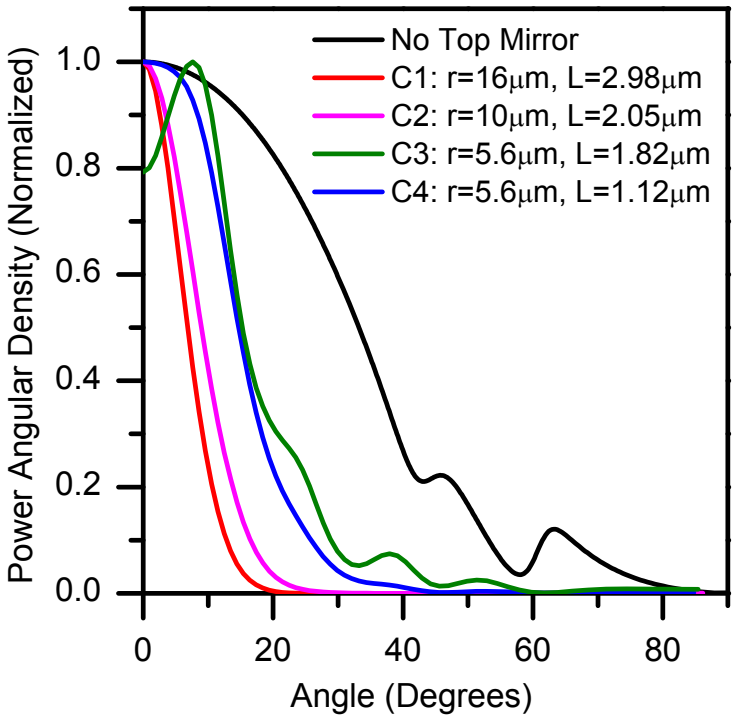

Figure 4: Dependence of emitted power per unit solid angle on observation angle in air for several cavities and without top mirror.

Effect of the concave DBR on the radiation pattern

Angular profiles for radiation from several cavities from Table 1 are presented in Fig. 4. We observe significant narrowing of the angular distribution for emitters in the cavities with concave mirrors compared to the case of a flat DBR only. The observed dependences for different cavities also agree with the qualitative notion that the larger cavity should give a more directional beam. Here we would like to discuss in more detail behavior of the cavity with the 5.6 μm radius mirror, as new features are observed in the radiation pattern for some mirror separations in this configuration.

Figures 3(e-f) correspond to the angular profiles presented in Fig. 4 for 5.6μm radius of curvature and 1.1μm and 1.8μm mirror separations. For the larger mirror separation we see an increase in the field amplitude in the planar regions adjacent to the curved mirror and simultaneously the appearance of extra non-zero wavevector components in the angular spectrum of upwards propagating radiation. These are accompanied by a drop in cavity

quality factor from 5500 to 4700 and an increase in the proportion of energy flowing through the side flux planes. The quality factor and sideways energy loss get worse with further increases in mirror separation, see Table 1 structure C5. It has been shown experimentally that the quality-factor in hemispherical cavities increases with increasing mirror separation up to a critical value where it begins to decrease.[3] This behaviour was attributed to a loss of mode stability which, in a purely geometrical picture, is where some rays at higher angles become able to exit the resonator on each round trip. Geometrical arguments predict that this occurs when the mirror separation is greater than the radius of curvature.[3] However, these arguments ignore the finite diameter of the curved section of the mirror. In the real system there is a sharply discontinuous interface between curved and planar regions which may cause scattering with a strength which depends on the local field amplitude. Qualitatively, the angular spread of the mode is dictated by the radius of curvature. The spatial extent of the beam at the top mirror will be proportional to this angular spread and the mirror separation. When the separation is large the spatial beam size will overlap the discontinuous region leading to scattering. It is likely that this scattering is the cause of the observed energy loss from the confined mode into sideways propagating modes and also of the complicated angular emission profile above the structure. The two effects together tend to reduce the fraction of power collected by the objective lens.

Finally, the fractions of total emitted power collected by the objective may be compared between the cavities and the case where there is no mirror (see main text and also Methods). For the cavities close to the experimental parameters C1 and C3 we expect to collect 5.3 and 2.2 times more of the total emission than in the case with no top mirror. This agrees with the qualitative notion that the larger cavity should give a more directional beam and so more of the emission should be collected.

Calculation of the Purcell enhancement

Further to the angular distribution, the FDTD method employed above can be used to calculate the effective mode volumes and Q-factors for the optical modes in the microcavity. We now discuss how these may be used to make an estimate of the Purcell factor. The enhancement of the spontaneous emission rate of an emitter at position $\boldsymbol{r_0}$ due to a cavity may be calculated using the standard formula[7]

$$F_P\left(\boldsymbol{r_0}\right) = \frac{3}{4\pi^2}\left(\frac{\lambda}{n\left(\boldsymbol{r_0}\right)}\right)^3\left(\frac{Q}{V_{eff}}\right) \tag{1}$$

Here λ is the vacuum wavelength, $\boldsymbol{r_0}$ is the position of the field maximum in the cavity and n is refractive index. The effective mode volume is given by

$$V_{eff} = \frac{\int_{-\infty}^{\infty}\int_0^{2\pi}\int_0^{\infty}\epsilon(\boldsymbol{r})\left|\boldsymbol{E}(\boldsymbol{r})\right|^2\cdot r\cdot dr d\phi dz}{\epsilon(\boldsymbol{r_0})\left|\boldsymbol{E}(\boldsymbol{r_0})\right|^2} \tag{2}$$

Here $\boldsymbol{r} = (r,\phi,z)$ is position in space and $\epsilon(\boldsymbol{r})\left|\boldsymbol{E}(\boldsymbol{r})\right|^2 = \epsilon(\boldsymbol{r})\left(\boldsymbol{E}(\boldsymbol{r})\cdot\boldsymbol{E}^*(\boldsymbol{r})\right)$ is the electric energy density. Since the full electromagnetic fields of the cavity modes are calculated as a function of position by the FDTD simulations the effective mode volumes are obtained simply by numerically performing the integral in equation 2. We obtain volumes of 6.46, 3.10 and 1.61 μm^3 for the cavities C1, C2 and C3 respectively.

Our FDTD calculations also give central wavelengths and Q-factors for the modes. These are obtained by examining the field in the cavity using a harmonic inversion technique.[6] For the cavities C1, C2 and C3 we obtain Q_1=11000, Q_2=7700 and Q_3=4700 respectively which lead to Purcell factors of F_{P1}=40.7, F_{P2}=59.4 and F_{P3}=69.8.

These Purcell factors provide an upper limit to the enhancement which may be achieved in a cavity. The actual ratio of spontaneous emission rates observed in an experiment will depend on the spectral and spatial overlap of the emitter with the optical mode which effect the local density of states and magnitude of the vacuum field respectively.[8] Accurate modeling of the experimentally observed cw PL enhancement and lifetime shortening in time-resolved

measurements also requires the knowledge of the non-radiative decay rates in the 2D film.

References

(1) Kretinin, A. V. et al. *Nano Letters* **2014**, *14*, 3270–3276.

(2) Dolan, P. R.; Hughes, G. M.; Grazioso, F.; Patton, B. R.; Smith, J. M. *Optics letters* **2010**, *35*, 3556–8.

(3) Dufferwiel, S.; Fras, F.; Trichet, A.; Walker, P. M.; Li, F.; Giriunas, L.; Makhonin, M. N.; Wilson, L. R.; Smith, J. M.; Clarke, E.; Skolnick, M. S.; Krizhanovskii, D. N. *Applied Physics Letters* **2014**, *104*, –.

(4) Novotny, L.; Hecht, B. *Principles of Nano-Optics*; Cambridge University Press, 2006.

(5) Lukosz, W. *J. Opt. Soc. Am.* **1979**, *69*, 1495.

(6) Oskooi, A. F.; Roundy, D.; Ibanescu, M.; Bermel, P.; Joannopoulos,; D., J.; Johnson, S. G. *Computer Physics Communications* **2010**, *181*, 687–702.

(7) Fox, M. *Quantum Optics, An Introduction*; Oxford University Press, 2006.

(8) Gérard, J. M.; Sermage, B.; Gayral, B.; Legrand, B.; Costard, E.; Thierry-Mieg, V. *Phys. Rev. Lett.* **1998**, *81*, 1110–1113.